



## Original Article

## On the use of low-dimensional temporal subspace constraints to reduce reconstruction time and improve image quality of accelerated 4D-MRI

Nikolai J. Mickevicius<sup>a,\*</sup>, Eric S. Paulson<sup>a,b,c</sup><sup>a</sup> Department of Radiation Oncology, Medical College of Wisconsin,; <sup>b</sup> Department of Radiology, Medical College of Wisconsin,; and <sup>c</sup> Department of Biophysics, Medical College of Wisconsin,

## ARTICLE INFO

## Article history:

Received 14 June 2020

Received in revised form 18 December 2020

Accepted 20 December 2020

Available online 5 January 2021

## Keywords:

4D-MRI

MRI reconstruction

MR-guided radiotherapy

SBRT

## ABSTRACT

**Background and purpose:** The purpose of this work is to investigate the use of low-dimensional temporal subspace constraints for 4D-MRI reconstruction from accelerated data in the context of MR-guided online adaptive radiation therapy (MRgOART).**Materials and methods:** Subspace basis functions are derived directly from the accelerated golden angle radial stack-of-stars 4D-MRI data. The reconstruction times, image quality, and motion estimates are investigated as a function of the number of subspace coefficients and compared with a conventional frame-by-frame reconstruction. These experiments were performed in five patients with four 4D-MRI scans per patient on a 1.5T MR-Linac.**Results:** If two or three subspace coefficients are used, the iterative reconstruction time is reduced by 32% and 18%, respectively, compared to conventional parallel imaging with compressed sensing reconstructions. No significant difference was found between motion estimates made with the subspace-constrained reconstructions ( $p > 0.08$ ). Qualitative improvements in image quality included reduction in apparent noise and reductions in streaking artifacts from the radial k-space coverage.**Conclusion:** Incorporating subspace constraints for accelerated 4D-MRI reconstruction reduces noise and residual undersampling artifacts in the images while reducing computation time, making it a strong candidate for use in clinical MRgOART workflows.

© 2021 Elsevier B.V. All rights reserved. Radiotherapy and Oncology 158 (2021) 215–223

## 1. Introduction

In stereotactic body radiotherapy (SBRT), ablative radiation doses are delivered to tumor targets over one to five fractions. With this technique, accurate daily delineations are critical to ensure precise delivery to the target while minimizing dose to nearby organs at risk (OARs). MR-guided online adaptive radiotherapy (MRgOART) on hybrid MRI/treatment machines, such as the Elekta Unity MR-Linac [1], permit treatment plan adaptations incorporating daily changes in geometry or motion prior to delivery of each treatment fraction. However, obtaining high quality daily reference images on which the adaptive plans are based can be challenging due to significant respiratory induced motion in the abdomen and thorax.

Recently, we detailed the implementation and initial clinical use of a 4D-MRI driven workflow for free-breathing abdominal SBRT on an Elekta Unity MR-Linac [2]. Currently, only free-breathing treatment deliveries are supported on Unity. The imple-

mentation of 4D-MRI was performed to eliminate systematic offsets between daily reference images and free-breathing treatment deliveries. Our approach employed a 3D golden angle radial [3] stack-of-stars [4] (GAR SoS) acquisition that is inherently robust against motion [5] and has favorable point spread function properties for recovery of artifact-free images from highly accelerated data acquisition periods [6,7].

The use of iterative algorithms is necessary for image recovery of highly accelerated data [8], which always come with a heavy computational burden. Using high performance computing helps to alleviate some of these issues [9], but trade offs between scan duration, reconstruction time, and image quality must be carefully made.

Most 4D methods consider the 4D-MRI reconstruction process as resolving completely separate images of the same anatomy in several motion states. An alternative approach considers 4D-MRI reconstruction as resolving the changes in each voxel's image intensity as a function of respiratory phase. The latter approach presents some interesting reconstruction possibilities. Over the average respiratory cycle, the image intensity within any given voxel will change slowly, or minimally in large homogeneous structures. This concept lends itself to a low-dimensional subspace

\* Corresponding author. Department of Human Oncology, University of Wisconsin-Madison, 600 Highland Ave, Madison, WI 53792, United States

E-mail address: [nmickevicius@wisc.edu](mailto:nmickevicius@wisc.edu) (N.J. Mickevicius).

representation of each voxel's signal evolution over respiratory phases. Constraining the reconstructed images to span a low-dimensional subspace with a rank less than the number of desired respiratory phases offers a lower computational complexity through the need for fewer 2D fast Fourier transform operations. The accuracy of the images, however, is dependent on an accurate selection of the basis functions. In the case of subspace-constrained reconstruction for resolving MR signal dynamics, basis functions are estimated by principal component analysis (PCA) of a dictionary of signal evolutions that were simulated via the Bloch equation [10–12]. In the case of resolving respiratory or cardiac motion, however, no analytical model exists for generation of subspace basis functions applicable to all patients. Rather, a low-resolution image navigator is acquired, from which the basis functions can be estimated via similar PCA methods [13–15]. Recent work by Feng et al. demonstrated that, for radial k-space coverage, the low-resolution navigator can be extracted directly from the full-resolution dataset to be reconstructed, thus eliminating any uncertainty between the acquisition of the navigator and imaging data [16,17]. This method was found to be profoundly successful for dynamic contrast-enhanced MRI applications. Here we assess the applicability of such methods for use in 4D-MRgOART.

The primary motivation for incorporating subspace constraints into the 4D-MRgOART workflow is reduced computational burden and, therefore, reconstruction time. The iterative methods necessary to reconstruct highly accelerated data require the use of many forward and adjoint Fourier transform operations. By approximating each voxel's signal evolution over respiratory phases as a low-dimensional subspace of rank  $K$ , the number of Fourier transform operations in each iteration reduces to  $K$  instead of the number of respiratory phases  $N_B$ . Further, subspace constraints improve the conditioning of the inverse problem provided the sampling of k-space produces incoherent artifacts over respiratory phases. This often results in improved image quality with the use of subspace-constrained reconstructions in addition to the computational efficiency benefits [18,10,15].

## 2. Methods

### 2.1. Image reconstruction

Raw k-space data from each 4D-MRI acquisition were transferred to an offline server (96 core Intel Xenon Platinum 2.7 GHz, 512 GB RAM) on the local Unity machine network where custom code written in MATLAB (The MathWorks, Natick, MA) automatically queues and processes each dataset. The data were pre-whitened to de-correlate inter-RF-coil noise [8,19], corrected for delays between gradients and data acquisition objects [20], brought to a hybrid image-k-space with an inverse Fourier transform along the Cartesian (superior/inferior) dimension, and coil sensitivity profiles were estimated slice-wise from all available k-space spokes using ESPIRiT [21]. Using an internally derived motion surrogate signal [22,9], each k-space spoke-plane was retrospectively sorted into one of ten respiratory bins based on a hybrid amplitude- and phase-based sorting. With this sorting method, the breathing surrogate was divided into five amplitude bins which are each split into inspiratory or expiratory phases based on the sign of the derivative of the surrogate signal at each point [23]. Bins one and six represent the extreme exhale and inhale phases, respectively. There was no constraint enforcing that each bin must have the same amount of data, therefore all acquired data were utilized in the reconstruction. With all slices reconstructed in parallel on the high performance server, 4D-MRI volumes were generated using conventional and subspace-constrained reconstruction algorithms as described below.

#### 2.1.1. Conventional reconstruction

Let  $\mathbf{x}_z \in \mathbb{C}^{N \times N \times N_B}$  be the reconstructed image for each slice  $z$ , where  $N$  is the in-plane matrix size and  $N_B$  is the number of respiratory bins. Given a coil sensitivity operator  $\mathbf{S}_z$ , a 2D non-uniform fast Fourier transform [24] operator  $\mathbf{F}$ , and the acquired multi-coil radial k-space data  $\mathbf{y}_z$ , the reconstructed image is obtained by minimizing the following cost function.

$$\underset{\mathbf{x}_z}{\text{minimize}} \quad \frac{1}{2} \left\| \sqrt{\mathbf{W}} \mathbf{F} \mathbf{S}_z \mathbf{x}_z - \sqrt{\mathbf{W}} \mathbf{y}_z \right\|_2^2 + \lambda \|\Psi \mathbf{x}_z\|_1 \quad (1)$$

Here,  $\sqrt{\mathbf{W}}$  is a density compensation operator multiplying each k-space spoke with the square root of a ramp filter. A regularization term promotes sparsity in the Wavelet domain with the use of an  $\ell_1$  norm penalty of the 2D Daubechies wavelet transform ( $\Psi$ ) of  $\mathbf{x}_z$  [25]. If  $\lambda$  is set to zero, the above problem is reduced to a conventional parallel imaging (SENSE) reconstruction [8].

#### 2.1.2. Estimation of subspace basis functions

Following the work by Feng et al. [16], we first perform an iterative reconstruction to obtain a low-resolution 4D-MRI using the fully sampled center of k-space. In our experience, there will typically be between 50 and 100 radial k-space spokes sorted into each k-space bin. Solving for the 4D-MRI time series from this amount of data is a far better conditioned inverse problem than solving for a time series using 13 spokes per frame as demonstrated in reference [16]. Therefore, we use a linear SENSE reconstruction to obtain the low-resolution 4D-MRI at matrix sizes of  $96 \times 96$  rather than performing the temporal total variation-regularized reconstruction. The signal evolutions for each voxel within the external patient contour are stacked into a matrix  $\mathbf{D} \in \mathbb{C}^{N_B \times N_V}$ , where  $N_V$  is the number of voxels in the mask. The external patient contour can be approximated automatically with thresholding of a motion-averaged image and binary mask operations. Using singular value decomposition (SVD), the signal evolutions can be represented as  $\mathbf{D} = \mathbf{u} \mathbf{\Sigma} \mathbf{v}^H$ . The first  $K$  columns of  $\mathbf{u}$  represent the most dominant basis functions that can be used to approximate the full signal evolution using a linear combination of the weighted basis functions.

#### 2.1.3. Subspace-constrained reconstruction

In contrast to the conventional reconstruction, the subspace-constrained reconstruction reconstructs subspace coefficient images  $\alpha_z \in \mathbb{C}^{N \times N \times K}$  for each slice. Then, an approximation of the 4D-MRI  $\mathbf{x}_z$  can be made by projecting each voxel through the subspace with a multiplication by the truncated matrix  $\mathbf{u}$  [10]. To achieve the aforementioned reductions in computational complexity made possible with subspace-constrained reconstructions, the implementation of the gridding and Fourier transform operators in this work were made following that described by Assländer et al [11]. We direct readers to this reference to understand how the “low-rank” NUFFT operator  $\tilde{\mathbf{F}}$  is implemented. The forward  $\tilde{\mathbf{F}}$  operator performs a single 2D FFT operation on each of the  $K$  subspace coefficient images followed by a sparse matrix multiplication with the subspace basis function-weighted k-space interpolation weights to obtain radial k-space data in the full respiratory phase domain. The inverse problem to solve for the subspace coefficient images is given by the following equation.

$$\underset{\alpha_z}{\text{minimize}} \quad \frac{1}{2} \left\| \sqrt{\mathbf{W}} \tilde{\mathbf{F}} \mathbf{S}_z \alpha_z - \sqrt{\mathbf{W}} \mathbf{y}_z \right\|_2^2 + \lambda \|\Psi \alpha_z\|_1 \quad (2)$$

This cost function is to be minimized using the same numerical optimization algorithm as the conventional reconstruction.

### 2.1.4. Numerical optimization details

If an operator  $\mathbf{A}$  representing either  $\sqrt{\mathbf{W}\mathbf{F}\mathbf{S}_z}$  or  $\sqrt{\mathbf{W}\mathbf{F}\mathbf{S}_z}$  acts on a variable  $\boldsymbol{\beta}$  representing  $\mathbf{x}_z$  or  $\boldsymbol{\alpha}_z$ , the above optimization problems can be generalized as

$$\underset{\boldsymbol{\beta}}{\text{minimize}} \quad \frac{1}{2} \|\mathbf{A}\boldsymbol{\beta} - \sqrt{\mathbf{W}\mathbf{y}_z}\|_2^2 + \lambda \|\boldsymbol{\Psi}\boldsymbol{\beta}\|_1. \quad (3)$$

Variable splitting poses this problem in the alternating direction method of multipliers (ADMM) form as

$$\begin{aligned} \underset{\boldsymbol{\beta}}{\text{minimize}} \quad & \frac{1}{2} \|\mathbf{A}\boldsymbol{\beta} - \sqrt{\mathbf{W}\mathbf{y}_z}\|_2^2 + \lambda \|\mathbf{z}\|_1 \\ \text{subject to} \quad & \boldsymbol{\Psi}\boldsymbol{\beta} - \mathbf{z} = \mathbf{0}. \end{aligned} \quad (4)$$

This yields the following algorithm to reconstruct  $\boldsymbol{\beta}$  at iteration  $j + 1$ :

$$\begin{aligned} \boldsymbol{\beta}^{j+1} &:= (\mathbf{A}^H \mathbf{A} + \rho \boldsymbol{\Psi}^H \boldsymbol{\Psi})^{-1} (\mathbf{A}^H (\sqrt{\mathbf{W}\mathbf{y}_z}) + \rho \boldsymbol{\Psi}^H (\mathbf{z}^j - \mathbf{u}^j)) \\ \mathbf{z}^{j+1} &:= S_{\lambda/\rho}(\boldsymbol{\Psi}\boldsymbol{\beta}^{j+1} + \mathbf{u}^j) \\ \mathbf{u}^{j+1} &:= \mathbf{u}^j + \boldsymbol{\Psi}\boldsymbol{\beta}^{j+1} - \mathbf{z}^{j+1} \end{aligned} \quad (5)$$

$\boldsymbol{\beta}^0$ ,  $\mathbf{z}^0$ , and  $\mathbf{u}^0$  are all initialized with zeros. Here  $S_{\lambda/\rho}$  is a sparsity promoting soft thresholding operator. See Boyd et al. for further information about the ADMM algorithm [26]. In each of the five iterations of the ADMM algorithm,  $\boldsymbol{\beta}^{j+1}$  was obtained using five iterations of a linear conjugate gradient algorithm. These numbers were chosen empirically along with values of  $\rho = 1$  and  $\lambda = 5 \times 10^{-3}$ . In the spirit of reproducible research, the MATLAB code to perform each of these reconstructions will be provided at <https://github.com/nmickevicius/Subspace4DMRI>.

### 2.1.5. Post processing

Following image reconstruction, the imaging volumes were interpolated to half of the prescribed slice thickness along the superior-inferior direction. A correction for gradient non-linearities (GNL) in 3D for each respiratory phase was performed using ReconFrame (GyroTools LLC, Zurich, Switzerland) with the GNL spherical harmonic coefficients obtained from the Unity system [27]. Mid-position (MidP) images [28] were generated using an optical flow deformable registration algorithm [29].

## 2.2. Imaging experiments

4D-MRI data acquired on a 1.5T MR-Linac (Unity, Elekta Instruments AB, Stockholm, Sweden) from five patients consenting to an institutional review board approved study were analyzed retrospectively. The 4D-MRI data were acquired as part of a pre-treatment imaging study. Four separate 4D-MRIs, each with different contrast (i.e. TFE, SPAIR TFE, bTFE, and SPAIR bTFE), were acquired for each patient using a Philips 3D Vane sequence (a GAR SoS sequence). TFE scans are predominantly  $T_1$ -weighted while the bTFE scans are  $T_2/T_1$ -weighted. SPAIR indicates the use of a spectrally selective inversion recovery method for fat signal suppression. The scan parameters for each of the contrasts are provided in the [Supplementary Material](#). Common parameters across all contrasts include a matrix size of  $256 \times 256$ , in-plane field-of-view of 420 mm, water-fat shift of 0.254 pixels, slice thickness of 4.76 mm, 44 acquired partitions, 80% partial Fourier, oversampling of 30% along the slice dimension, and two parallel spatial saturation (REST) slabs. The standard 8-channel (4 anterior, 4 posterior) coil array was used for signal reception. For each contrast, five 4D-MRI studysets were reconstructed (i.e. one conventional reconstruction, and four subspace reconstructions with  $K \in [2, 3, 4, 5]$ ).

### 2.2.1. Reconstruction time comparison

For each value of  $K$ , three time comparisons were made relative to the conventional reconstruction. First, the “4D Reconstruction Time” required to perform the iterative ADMM algorithm was compared. This includes the time to calculate the basis functions for subspace-constrained reconstructions. Second, the “time-to-MidP” required to produce MidP images was compared. This includes the time to load and pre-process the data, estimate coil sensitivity profiles, perform the iterative reconstruction, perform GNL correction, write DICOM images, and transfer the images to the treatment planning system. Finally, the “time-to-binned 4D” required to produce binned 4D images was compared. Although the MidP image is derived from the binned 4D images, the MidP images serve as the reference for the daily adaptive plan, and, thus, producing the MidP images first enables the adaptive planning process to start in the shortest time interval possible [2]. The mean 4D reconstruction times from all values of  $K$  were compared to those of the conventional reconstruction using a paired t-test.

### 2.2.2. Image quality comparisons

Qualitative image quality assessments were performed for all reconstructions and contrasts across all subjects. The first comparison involved an overall assessment of image quality by two experienced MR physicists including image features such as noise, sharpness, and artifacts from data undersampling. The second comparison assessed the quality of the MidP images for the  $K = 2$  and  $K = 3$  reconstructions compared with the conventional reconstructions for all subjects and contrasts. The MidP images were compared in the reformatted coronal plane to visualize the sharpness of each MidP image along the primary axis of respiratory motion (i.e. the superior/inferior direction).

### 2.2.3. Motion assessment

Since the use of GAR-SoS-based 4D-MRI has been well validated in the context of MR-guided radiation therapy [30,9,31,2], the conventional reconstruction was used as a reference for anatomical position within each respiratory phase. The position of the top of the right kidney along the superior/inferior dimension was noted within each phase for each reconstruction. For each value of  $K$ , the hypothesis of no significant difference in anatomical position between the conventional and subspace-constrained reconstructions was tested with a paired t-test with a significance level of 0.05.

## 3. Results

The image reconstruction time comparisons are summarized in [Fig. 1](#). For each reconstruction type, a total of 12 data points were included (i.e. four contrasts for five subjects). The mean reconstruction time (“4D Recon. Time”) includes the iterative reconstruction time spent performing the ADMM algorithm for each 4D-MRI reconstruction. For the subspace-constrained reconstructions, the time to calculate the subspace basis functions is also shown. The mean 4D reconstruction time of 3.25 min for  $K = 2$  reconstructions was significantly faster than the 6.67 min of the conventional reconstruction ( $p < 1e-8$ ). Only the  $K = 2$  subspace-constrained reconstruction times were statistically significantly lower than the conventional reconstruction times. The “time-to-MidP” results are shown in the second column for each reconstruction. Finally, the “time-to-binned 4D” results are shown in the third column for each reconstruction group. The “time-to-MidP” and “time-to-binned 4D” results for the  $K = 2$  and  $K = 3$  reconstructions were shorter than the conventional reconstruction times in every case tested. The mean time required to estimate the sub-

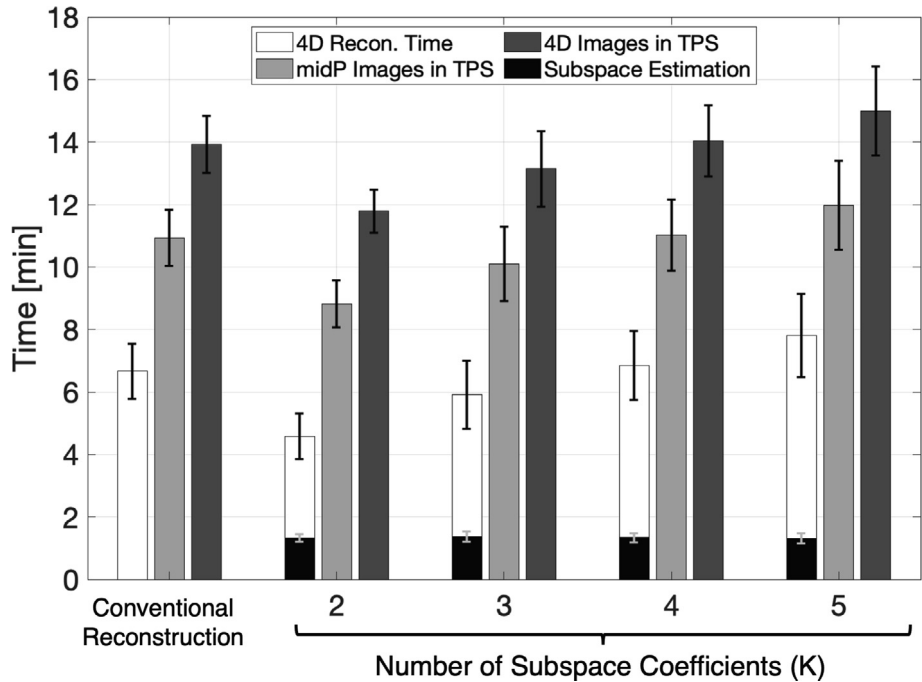


**Fig. 1.** Reconstruction time comparison. Each group of three bars represents a different reconstruction algorithm. The first bar in each group represents the mean iterative reconstruction time. For subspace reconstructions, the portion of this time taken up by estimating the subspace basis functions is also shown. The second bar represents the mean “time-to-MidP”. The third bar represents the mean “time-to-binned 4D”. The error bars denote standard deviation.

space basis functions of 1 min 21 s was consistent for all reconstructions.

Three-plane (i.e. axial, sagittal, and coronal) views of each 4D-MRI reconstruction algorithm are shown in the end-inspiratory

phase in [Figs. 2,3](#) for two subjects for the contrast selected by the treating physician. Orthogonal crosshairs overlaid on each image intersect the tumor target. For all values of  $K$ , the subspace-constrained reconstruction reduced the intensity of the

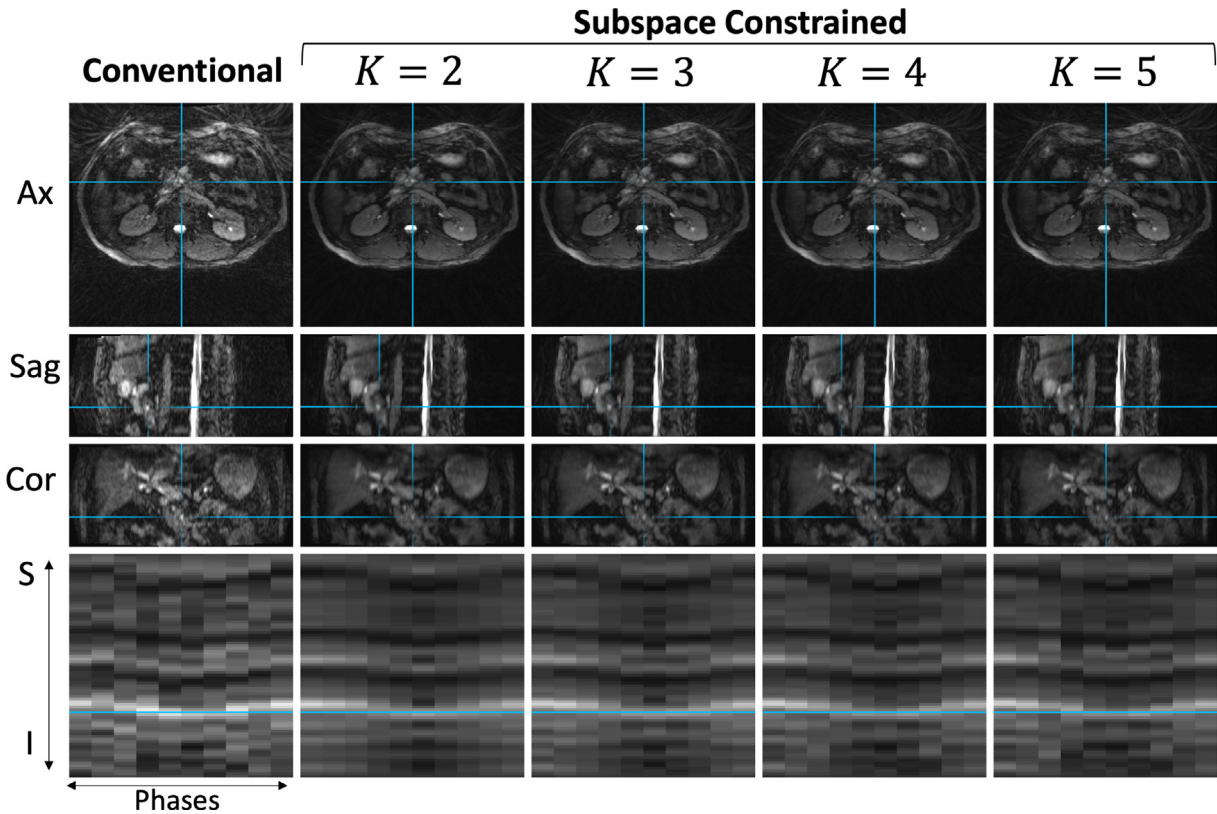


**Fig. 2.** Three-plane views of the inspiratory phase from each of the reconstruction algorithms for the SPAIR bTFE 4D-MRI acquisition for Subject 1. The bottom row in the figure also shows a plot of a one-dimensional image along the superior (S)/inferior (I) dimension for each of the 10 respiratory phases.



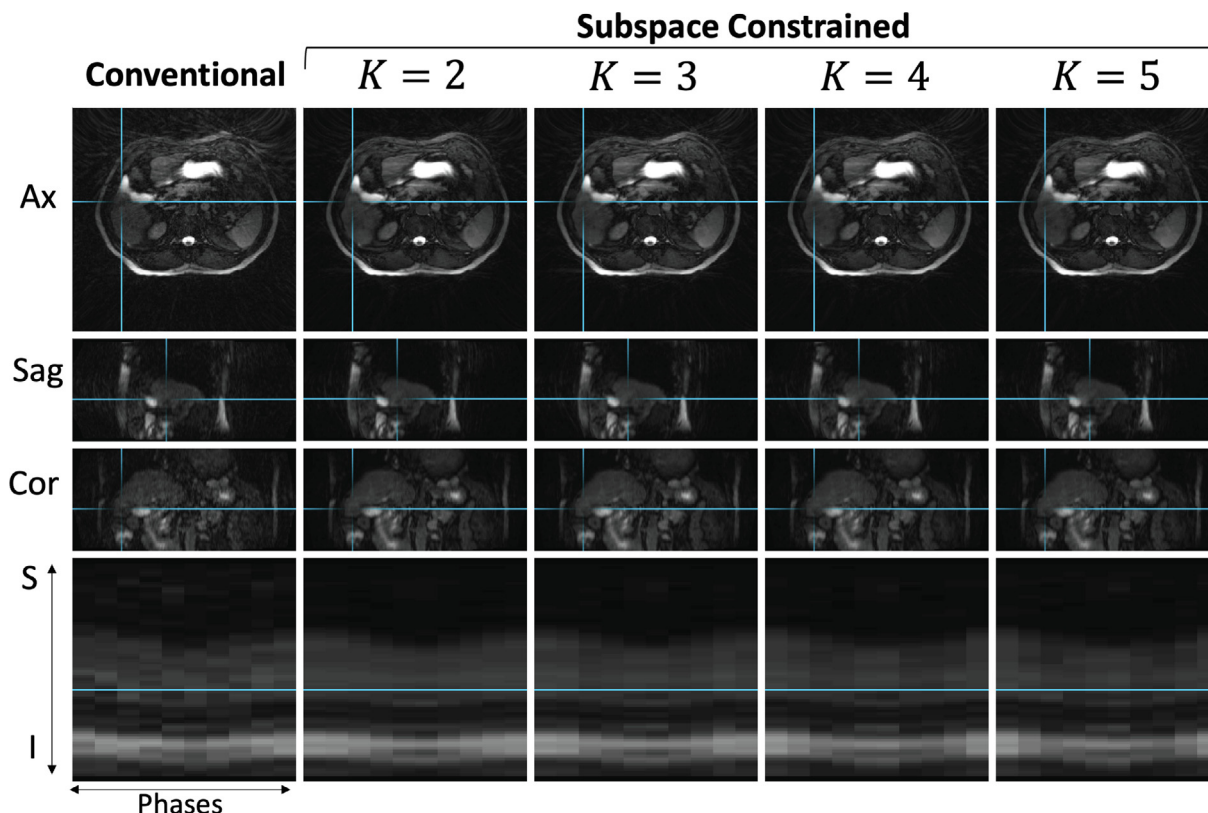


**Fig. 3.** Three-plane views of the inspiratory phase from each of the reconstruction algorithms for the SPAIR bTFE 4D-MRI acquisition for Subject 2. The bottom row in the figure also shows a plot of a one-dimensional image along the superior (S)/inferior (I) dimension for each of the 10 respiratory phases.

residual undersampling artifacts and noise enhancement. The reduction in streaking artifacts are best viewed in the axial plane. The streaks originate in the patient, extend outward, and appear to bend toward the image peripheries due to the applied gradient non-linearity correction. Higher values of  $K$  (i.e. 4–5), appear to amplify streak artifacts compared to lower values of  $K$  (i.e. 2–3). In the bottom row of Figs. 2,3, a one-dimensional image along the superior/inferior dimension across each of the 10 respiratory phases are shown. These projections intersect the target along the crosshairs shown in the upper portion of the figures. A line indicating the position of the axial slice from each figure is plotted over the projections to use as a reference for visualizing the amount of respiratory motion resolved within each reconstruction method. Additionally, due to the reduced noise in the images, the motion throughout the average respiratory cycles appears smoother in the projections. Video files demonstrating motion in three-planes for all subjects can be found in the [Supplementary Information](#).

A coronal reformat of the MidP images from conventional,  $K = 2$ , and  $K = 3$  reconstructions for three subjects and all contrasts are shown in Fig. 4. Only the  $K = 2$  and  $K = 3$  subspace-constrained reconstructions are shown since they alone provided a decrease in computation time compared with the conventional reconstruction (See Fig. 1). In general, the overall MidP image quality is similar between the conventional and  $K = 2$  images. In some cases (e.g. the TFE and SPAIR TFE contrasts for Subject 2), the  $K = 3$  images are slightly less blurred at the lung liver interface. Sharper visualization of blood vessels in the liver can be seen in Subject 3 for both the  $K = 2$  and  $K = 3$  reconstructions compared with the conventional.

Additionally, the  $K = 2$  subspace-constrained reconstructions are shown for the third subjects for all contrasts at expiration in Fig. 5. A similar figure for the first and second subjects can be seen

in [Supplementary Material Figs. S1 and S2](#). For all contrasts, the  $K = 2$  reconstruction is able to resolve respiratory motion as demonstrated with the superior/inferior image intensity projections. The amplitude of the motion appears consistent over the four contrasts acquired for each patient. Consistently high SNR images for each subject can be seen with the  $K = 2$  reconstructions, regardless of contrast.

The mean difference between the position of the right kidney measured using the conventional and subspace-constrained reconstructions are shown for all values of  $K$  and respiratory phases in Fig. 6. Twenty data points contributed to the mean and standard deviation for each reconstruction (i.e. 5 subjects, 4 contrasts). As seen in the figure, the mean difference in each patients' kidney along the superior/inferior dimension is less than 0.75 mm in all cases. For all values of  $K$ , no significant differences in motion estimates were found between conventional and subspace reconstructions ( $p$ -values were 0.10, 0.14, 0.08, and 0.16 for  $K = 2, K = 3, K = 4$ , and  $K = 5$ , respectively). The largest difference between motion estimates among all data was 2.49 mm, which is approximately half of the acquired slice thickness. For the  $K = 2$  reconstructions, the mean difference in position was less than 0.5 mm in all respiratory phases.

#### 4. Discussion

Temporal subspace-constrained image reconstruction was implemented and tested in the context of 4D-MRgOART. A subspace-constrained reconstruction with two or three basis functions yielded lower reconstruction times, fewer image artifacts, sharper mid-position images, and similar motion estimates compared with conventional bin-by-bin 4D-MRI reconstructions. Subspace constraints provided all of these benefits for five patients across four different image contrasts. These results demonstrate

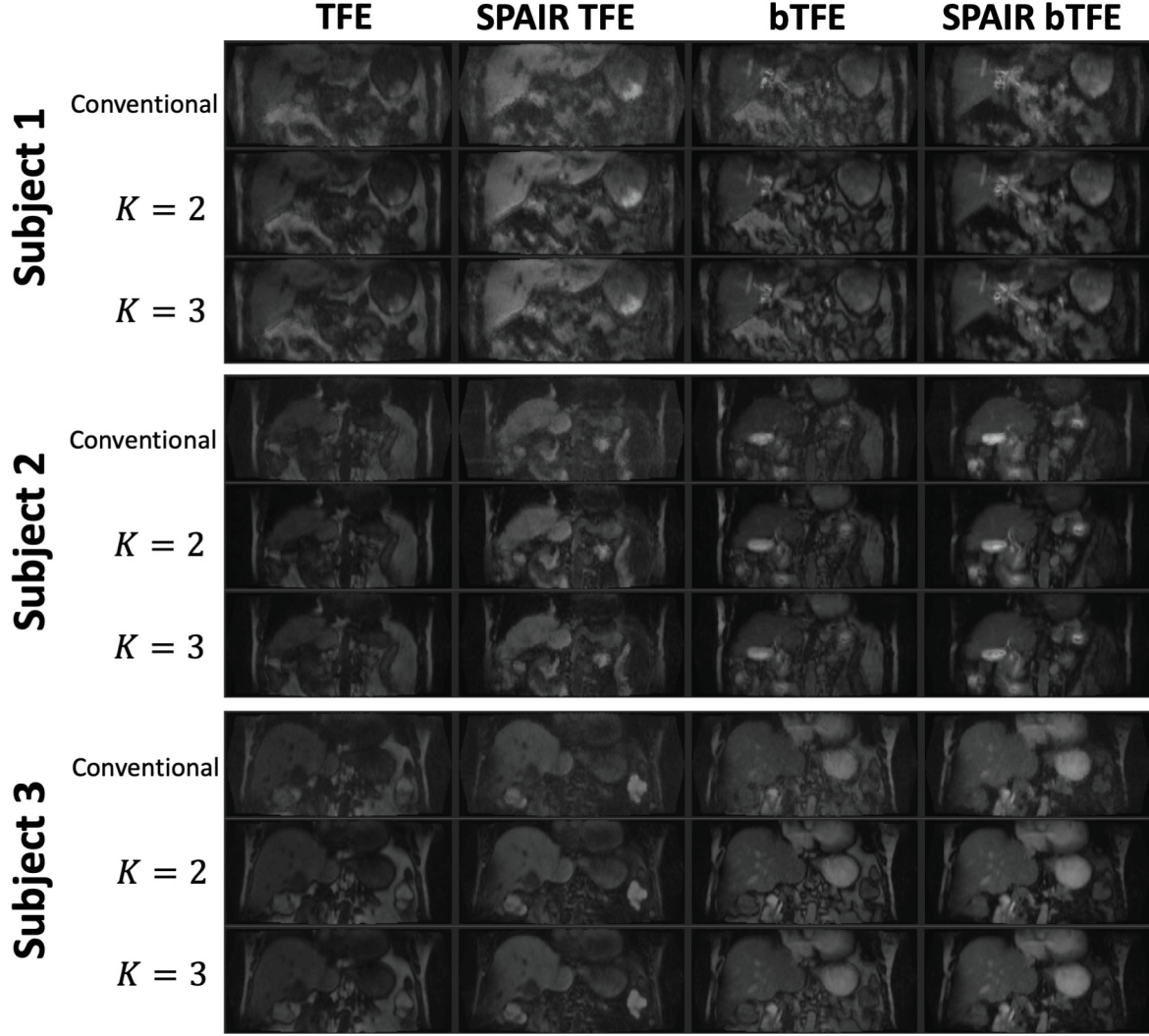


Fig. 4. Coronal reformat of the conventional,  $K = 2$ , and  $K = 3$  mid-position volumes for Subjects 1–3 and all image contrasts.

the advantages of incorporating subspace constraints in highly accelerated 4D-MRI reconstructions.

In the present work, the impact on reconstruction time and 4D-MRI image quality by varying the number of subspace coefficients was thoroughly tested. There are other variables associated with subspace-constrained reconstructions that were held constant throughout these experiments. The matrix size of the low resolution images used to calculate the subspace basis functions was fixed at  $96 \times 96$  [16]. Lowering this to  $64 \times 64$  would certainly reduce computation time, but would have an unknown impact on image quality. Further, the basis functions were estimated using all voxels within the outer contour of the patient. Since, in our implementation, all slices are treated individually, a slice-dependent calculation of the basis functions could be performed. The impact of both of these variables will be investigated in future work.

The subspace-constrained reconstructions improved image quality for all available contrasts while using a rapid steady-state gradient echo sequence.  $T_1$  and  $T_2/T_1$  weighting can be achieved using spoiled and balanced gradient echo acquisitions, respectively. The fat suppressed turbo field echo (SPAIR TFE) contrast usually results in very noisy 4D-MRI volumes due to the inherently low SNR compounded with high levels of undersampling, but the subspace constraints were effective at suppressing the noise. The anterior side of the SPAIR TFE images appears hyperintense. This

artifact does not appear to be an artifact of the subspace-constrained reconstruction since the conventional reconstruction exhibits this characteristic as well. Artifacts may further arise from very few spokes being sorted into the inspiration respiratory phase due to breathing inconsistencies and the highly accelerated data acquisition period. In these cases, the low resolution images used to estimate the subspace basis functions are still corrupted by undersampling artifacts which then propagate into the subspace constrained reconstruction. This effect can be seen in Supplementary Material video titled 'Subj1-5\_K2\_4DMRI\_v2.mp4'. The reference reconstructions in these bins are also severely corrupted by streaking artifacts. This effect can be suppressed by using a fewer number of respiratory phases.

One limitation of the 3D Vane sequence used in this work is that pure  $T_2$  weighted 4D-MRI [32] imaging cannot be acquired with such gradient echo methods. To maintain the advantages of the GAR-SoS data sampling, perhaps a future implementation using a 3D variable flip angle fast spin echo approach [33,34] could be employed to resolve respiratory motion with  $T_2$  contrast. This would, however, come at the expense of longer scan times due to the necessarily long repetition time to allow for  $T_1$  recovery between fast spin echo segments.

The use of iterative methods for 4D-MRI reconstructions can be avoided altogether if the scan durations approach 10 min. In our

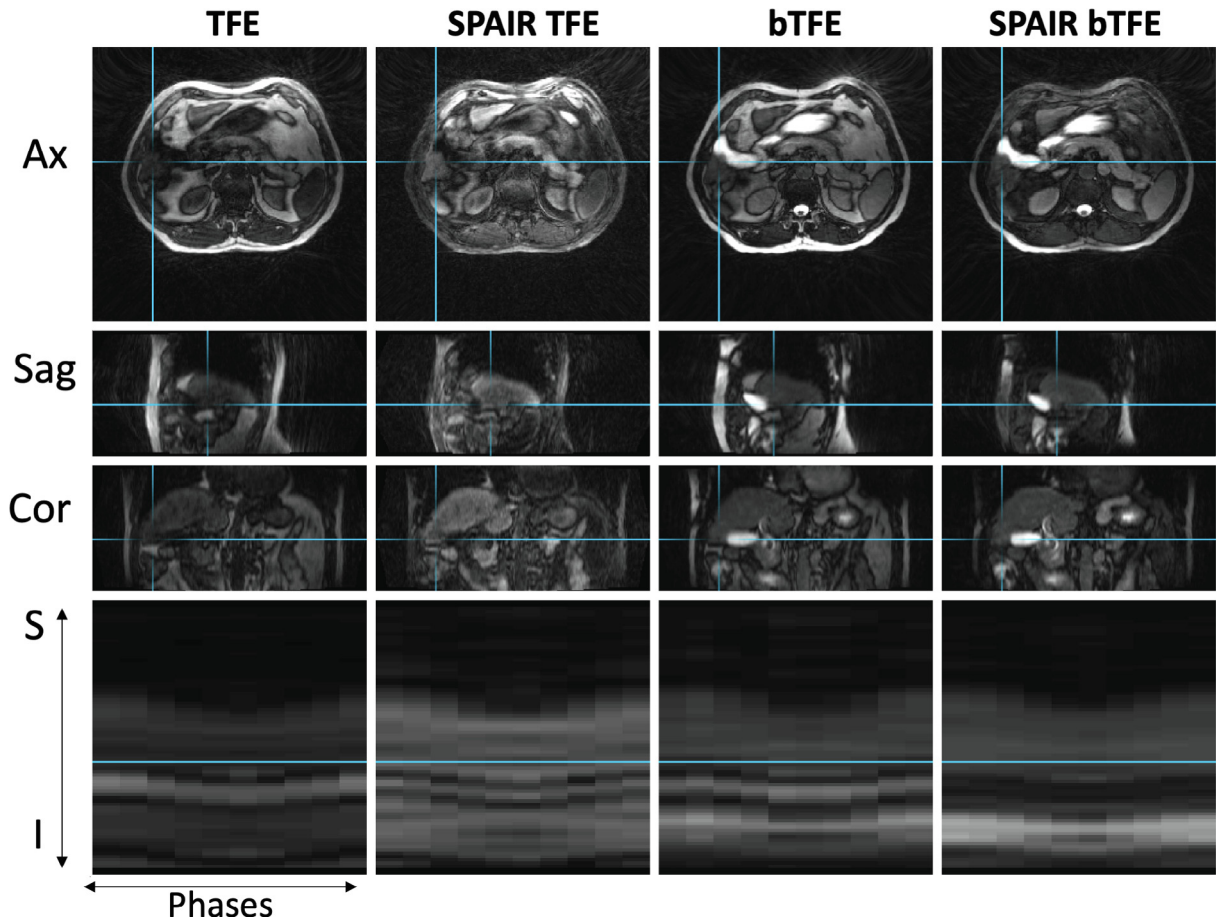


**Fig. 5.** Three-plane views of the expiratory phase from the  $K = 2$  reconstructions of each of the four contrasts for Subject 3. The bottom row in the figure also shows a plot of a one-dimensional image along the superior (S)/inferior (I) dimension for each of the 10 respiratory phases.

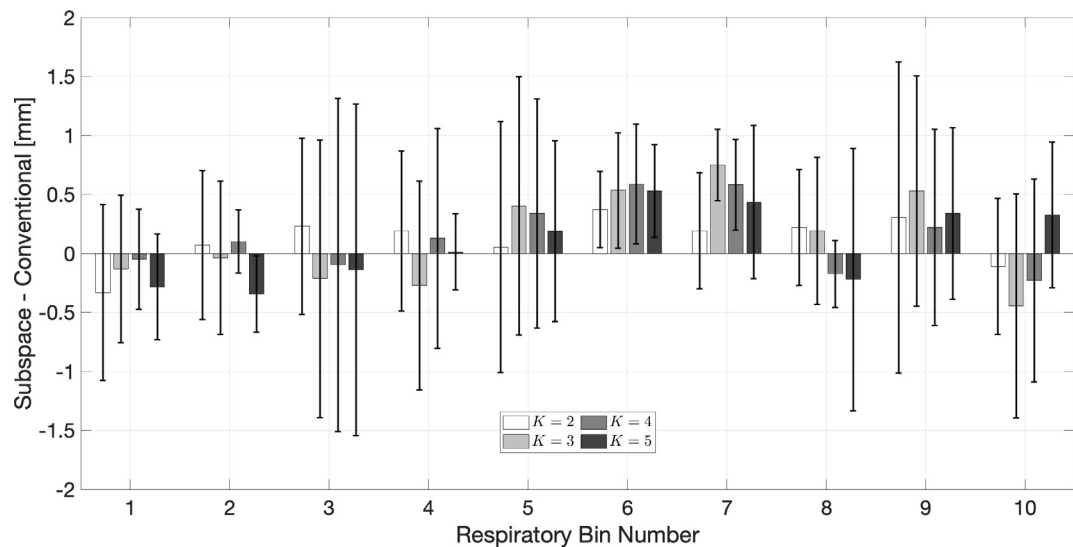


**Fig. 6.** Mean difference in the position of the right kidney along the superior/inferior dimension for each respiratory phase and value of  $K$ . Twenty data points contributed to the mean and standard deviation for each reconstruction (5 subjects, 4 contrasts).

Institution, we choose to employ highly accelerated 4D-MRI acquisitions (about 3.5 min) as a compromise between image quality and minimizing the time before the adaptive planning process can begin. Once the 4D-MRI data are sent to the server for reconstruction, a battery of quantitative imaging is acquired including

intravoxel incoherent motion (IVIM) [35], variable flip angle  $T_1$  [36], and fast spin echo-based  $T_2$  mapping [37]. These parameters may correlate with response to radiation therapy, and acquiring them longitudinally during each fraction may provide further insight into the efficacy of a particular treatment regimen. Thus,



acquiring a 4D-MRI scan in as little time as possible presents opportunities for future use of SBRT plan adaptations based on geometry, motion, and biological imaging biomarkers.

While constraining signal intensity variations to span a low-dimensional subspace is more similar to temporal regularization than conventional spatially regularized compressed sensing reconstructions, an explicit comparison with XD-GRASP as a reference method was avoided for several reasons. First, in our experience, consistent image quality and motion estimates for all patients with a single total variation regularization parameter cannot be guaranteed. For patients with large respiratory motion amplitudes, small regularization parameters do not remove enough streaking artifacts, and large regularization parameters can cause underestimation of respiratory motion [22,38,9]. Excellent image quality and motion accuracy can be obtained with XD-GRASP if parameter tuning is performed on a case-by-case basis, but this is not feasible for online RT treatment guidance. Second, we have observed that XD-GRASP performs best when a non-linear conjugate gradient (CG) algorithm is used to solve for the binned images. This method requires a backtracking line search which involves computing the forward model many times within each iteration. The ADMM algorithm uses soft thresholding operations between linear CG updates, making it a much more efficient solver compared to non-linear CG. Again, in our experience, using ADMM to solve the XD-GRASP optimization problem does not provide sufficient improvements in image quality. Since using non-linear CG yields infeasible reconstruction times (approximately 9 min of computation to iteratively solve for the 4D-MRI volume), we have never deemed it feasible for online 4D-MRI guidance. As such, we used a conventional wavelet regularized reconstruction with ADMM as a reference method for comparison with the subspace-constrained reconstructions.

The assessment of motion accuracy was limited to the comparison of superior-inferior motion of the kidney in all subjects between conventional and subspace-constrained reconstructions. Ideally, Dice coefficients of similarity between tumor contours in each phase would be compared across image reconstruction methods. However, gradient echo (GRE) imaging does not always provide direct visualization of the gross tumor volume. Particularly, pancreatic lesions may be difficult to visualize with GRE imaging without intravenous contrast. The goal of 4D imaging in these cases is to confirm the position of nearby organs at risk after propagation of contours from a reference studyset. Thus, since not all patients' tumors had the same OAR, an organ visible in all subjects and on all four image contrasts was chosen for the motion analysis.

While the time saving benefits of subspace-constrained reconstructions over conventional reconstructions have been demonstrated in this work, further reduced reconstruction times are still desired. In efforts to further reduce the computation time, the subspace-constrained 4D-MRI reconstruction algorithm is currently being configured to run using the open source Berkeley Advanced image Reconstruction Toolbox (BART, <https://mrirecon.github.io/bart/>) on graphics processing units (GPU) to make use of their vastly hyperthreaded capabilities. The implementation in BART will also facilitate cooperative 4D-MRI research between institutions with a Unity system. If even lower scan times than those proposed here are desired, the use of deep learned image priors could be employed to recover diagnostic quality images from extremely undersampled k-space data [39,40].

While the use of two subspace coefficients may be desirable from image quality and reconstruction time viewpoints for 4D-MRgOART, higher numbers subspace coefficients may be desirable for use in 4D-MRI reconstructions obtained during MR simulation for reference plan generation. Reference plan generation does not have the same time requirements as the online environment, and

use of additional subspace coefficients may better retain the capability of resolving non-uniform motion throughout the imaging volume.

We have demonstrated here the novel incorporating of temporal subspace constraints 4D-MRI reconstruction for online adaptive MR-guided radiotherapy. Temporal subspace constraints reduce reconstruction times and improve image quality compared with conventional bin-by-bin 4D-MRI reconstructions without sacrificing precision in motion estimation. Estimation of the subspace basis functions does not require any additional navigator acquisitions; the subspace basis functions can be estimated using low resolution reconstructions directly from the full resolution data. The reduction of noise and improved sharpness in the MidP images with the use of subspace-constrained reconstructions will be beneficial for free-breathing 4D-MRgOART workflows.

## Declaration of Competing Interest

The authors declare that they have no known competing financial interests or personal relationships that could have appeared to influence the work reported in this paper.

## Acknowledgements

The authors would like to thank Cathy Marszalkowski for her efforts with IRB protocol submission and consenting patients.

## Appendix A. Supplementary data

Supplementary data associated with this article can be found, in the online version, at <https://doi.org/10.1016/j.radonc.2020.12.032>.

## References

- [1] Lagendijk JJ, Raaymakers BW, van Vulpen M. The magnetic resonance imaging linac system. *Semin Radiat Oncol* 2014;243:207–9.
- [2] Paulson ES, Ahunbay E, Chen X, Mickevicius NJ, Chen GP, Schultz C, Erickson B, Straza M, Hall WA, Li XA. 4D-MRI driven MR-guided online adaptive radiotherapy for abdominal stereotactic body radiation therapy on a high field MR-Linac: implementation and initial clinical experience. *Clin Transl Radiat Oncol* 2020;23:72–9.
- [3] Winkelmann S, Schaeffter T, Koehler T, Eggers H, Doessel O. An optimal radial profile order based on the Golden Ratio for time-resolved MRI. *IEEE Trans Med Imaging* 2007;261:68–76.
- [4] Block KT, Chandarana H, Milla S, Bruno M, Mulholland T, Fatterpekar G, Hagiwara M, Grimm R, Geppert C, Kiefer B, et al. Towards routine clinical use of radial stack-of-stars 3D gradient-echo sequences for reducing motion sensitivity. *J Korean Soc Magn Resonance Med* 2014;182:87–106.
- [5] Glover GH, Noll DC. Consistent projection reconstruction (CPR) techniques for MRI. *Magn Resonance Med* 1993;293:345–51.
- [6] Block KT, Uecker M, Frahm J. Undersampled radial MRI with multiple coils. Iterative image reconstruction using a total variation constraint. *Magn Reson Med* 2007;576:1086–98.
- [7] Feng L, Grimm R, Block KT, Chandarana H, Kim S, Xu J, Axel L, Sodickson DK, Otazo R. Golden-angle radial sparse parallel MRI: combination of compressed sensing, parallel imaging, and golden-angle radial sampling for fast and flexible dynamic volumetric MRI. *Magn Reson Med* 2014;723:707–17.
- [8] Pruessmann KP, Weiger M, Börner P, Boesiger P. Advances in sensitivity encoding with arbitrary k-space trajectories. *Magn Reson Med* 2001;464:638–51.
- [9] Mickevicius N, Paulson E. Investigation of undersampling and reconstruction algorithm dependence on respiratory correlated 4D-MRI for online MR-guided radiation therapy. *Phys Med Biol* 2017;628.
- [10] Tamir JJ, Uecker M, Chen W, Lai P, Alley MT, Vasanawala SS, Lustig M. T<sub>2</sub>-shuffling: sharp, multicontrast, volumetric fast spin echo imaging. *Magn Reson Med* 2017;771:180–95.
- [11] Assländer J, Cloos MA, Knoll F, Sodickson DK, Hennig J, Lattanzi R. Low rank alternating direction method of multipliers reconstruction for MR fingerprinting. *Magn Reson Med* 2018;791:83–96.
- [12] Zhao B, Setsompop K, Adalsteinsson E, Gagoski B, Ye H, Ma D, Jiang Y, Ellen Grant P, Griswold MA, Wald LL. Improved magnetic resonance fingerprinting reconstruction with low-rank and subspace modeling. *Magn Reson Med* 2018;792:933–42.



- [13] Pedersen H, Kozerke S, Ringgaard S, Nehrke K, Kim WY. k-t PCA: temporally constrained k-t BLAST reconstruction using principal component analysis. *Magn Reson Med* 2009;623:706–16.
- [14] Fu M, Zhao B, Carignan C, Shosted RK, Perry JL, Kuehn DP, Liang ZP, Sutton BP. High-resolution dynamic speech imaging with joint low-rank and sparsity constraints. *Magn Reson Med* 2015;735:1820–32.
- [15] Christodoulou AG, Shaw JL, Nguyen C, Yang Q, Xie Y, Wang N, Li D. Magnetic resonance multitasking for motion-resolved quantitative cardiovascular imaging. *Nat Biomed Eng* 2018;24:215–26.
- [16] Feng L, Wen Q, Huang C, Tong A, Liu F, Chandarana H. GRASP Pro: imProving GRASP DCE MRI through self calibrating subspace modeling and contrast phase automation. *Magn Reson Med* 2020;831:94–108.
- [17] Feng L, Tyagi N, Otazo R. MRSIGMA: Magnetic Resonance SIGnature MAtching for real-time volumetric imaging. *Magn Reson Med* 2020;843:1280–92.
- [18] Lam F, Liang ZP. A subspace approach to high-resolution spectroscopic imaging. *Magn Reson Med* 2014;714:1349–57.
- [19] Kellman P, McVeigh ER. Image reconstruction in SNR units: a general method for SNR measurement. *Magn Reson Med* 2005;546:1439–47.
- [20] Krämer M, Biermann J, Reichenbach JR. Intrinsic correction of system delays for radial magnetic resonance imaging. *Magn Reson Imaging* 2015;334:491–6.
- [21] Uecker M, Lai P, Murphy MJ, Virtue P, Elad M, Pauly JM, Vasanawala SS, Lustig M. ESPIRiT—an eigenvalue approach to autocalibrating parallel MRI: Where SENSE meets GRAPPA. *Magn Reson Med* 2014;713:990–1001.
- [22] Feng L, Axel L, Chandarana H, Block KT, Sodickson DK, Otazo R. XD-GRASP: golden-angle radial MRI with reconstruction of extra motion-state dimensions using compressed sensing. *Magn Reson Med* 2016;752:775–88.
- [23] Liang X, Yin FF, Liu Y, Cai J. A probability-based multi-cycle sorting method for 4D-MRI: a simulation study. *Med Phys* 2016;4312:6375–85.
- [24] Fessler J, Sutton B. Nonuniform fast fourier transforms using min-max interpolation. *IEEE Trans Signal Process* 2003;512:560–74.
- [25] Lustig M, Donoho D, Pauly JM. Sparse MRI: the application of compressed sensing for rapid MR imaging. *Magn Reson Med* 2007;586:1182–95.
- [26] Boyd S, Parikh N, Chu E, Peleato B, Eckstein J. Distributed optimization and statistical learning via the alternating direction method of multipliers. *Foundations and trends. Mach Learn* 2010;31:1–122.
- [27] Janke A, Zhao H, Cowin GJ, Galloway GJ, Doddrell DM. Use of spherical harmonic deconvolution methods to compensate for nonlinear gradient effects on MRI images. *Magn Reson Med* 2004;521:115–22.
- [28] Wolthaus J, Sonke JJ, Van Herk M, Damen E. Reconstruction of a time-averaged midposition CT scan for radiotherapy planning of lung cancer patients using deformable registration a. *Med Phys* 2008;359:3998–4011.
- [29] Horn B, Schunck B. Determining optical flow. *Artif Intell* 1981;17:185–203.
- [30] Stemkens B, Tijssen RH, de Senneville BD, Heerkens HD, van Vulpen M, Lagendijk JJ, van den Berg CA. Optimizing 4-dimensional magnetic resonance imaging data sampling for respiratory motion analysis of pancreatic tumors. *Int J Radiat Oncol Biol Phys* 2015;913:571–8.
- [31] Stemkens B, Paulson ES, Tijssen RH. Nuts and bolts of 4D-MRI for radiotherapy. *Phys Med Biol* 2018;6321:2101..
- [32] Freedman JN, Collins DJ, Bainbridge H, Rank CM, Nill S, Kachelrieß M, Oelfke U, Leach MO, Wetscherek A. T2-weighted 4D magnetic resonance imaging for application in magnetic resonance-guided radiotherapy treatment planning. *Invest Radiol* 2017;5210:563–73.
- [33] Mugler III JP. Optimized three-dimensional fast-spin-echo MRI. *J Magn Reson Imaging* 2014;394:745–67.
- [34] Benkert T, Mugler JP, Riegler DS, Sodickson DK, Chandarana H, Block KT. Hybrid  $T_2$  and  $T_1$  weighted radial acquisition for free breathing abdominal examination. *Magn Reson Med* 2018;805:1935–48.
- [35] Le Bihan D, Breton E, Lallemand D, Aubin M, Vignaud J, Laval-Jeantet M. Separation of diffusion and perfusion in intravoxel incoherent motion MR imaging. *Radiology* 1988;1682:497–505.
- [36] Deoni SC, Rutt BK, Peters TM. Rapid combined  $T_1$  and  $T_2$  mapping using gradient recalled acquisition in the steady state. *Magn Reson Med* 2003;493:515–26.
- [37] Ben-Eliezer N, Sodickson DK, Block KT. Rapid and accurate  $T_2$  mapping from multi-spin-echo data using Bloch-simulation-based reconstruction. *Magn Reson Med* 2015;732:809–17.
- [38] Rank CM, Heußner T, Buzan MT, Wetscherek A, Freitag MT, Dinkel J, Kachelrieß M. 4D respiratory motion-compensated image reconstruction of free-breathing radial MR data with very high undersampling. *Magn Reson Med* 2017;773:1170–83.
- [39] Aggarwal HK, Mani MP, Jacob M. MoDL: model-based deep learning architecture for inverse problems. *IEEE Trans Med Imaging* 2018;382:394–405.
- [40] Hammernik K, Klatzer T, Kobler E, Recht MP, Sodickson DK, Pock T, Knoll F. Learning a variational network for reconstruction of accelerated MRI data. *Magn Reson Med* 2018;796:3055–71.